Available online at www.sciencedirect.com

ScienceDirect

journal homepage: www.elsevier.com/locate/he

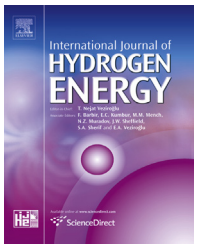

Development of potential organic-molecule-based hydrogen storage materials: Converting C–N bond-breaking thermolysis of guanidine to N–H bond-breaking dehydrogenation

Xiuquan Zhou [a], *Wei Zhou* [b], *Terrence J. Udovic* [b], *Taner Yildirim* [b], *John J. Rush* [b,c], *Efrain E. Rodriguez* [a], *Hui Wu* [b,*]

[a] *Department of Chemistry & Biochemistry, University of Maryland, College Park, MD, 20742-4454, USA*
[b] *NIST Center for Neutron Research, National Institute of Standards and Technology, Gaithersburg, MD, 20899-6102, USA*
[c] *Department of Materials Science and Engineering, University of Maryland, College Park, MD, 20742-2115, USA*

ARTICLE INFO

Article history:
Received 22 December 2015
Received in revised form
18 August 2016
Accepted 22 August 2016
Available online 8 September 2016

Keywords:
Hydrogen storage
Endothermic dehydrogenation
Crystal structure determination
Guanidine
Metal guanidinates

ABSTRACT

The small organic molecule guanidine CN_3H_5 can be anionized via a facile reaction with alkali-metal hydrides or amides with the formation of metal guanidinates (MCN_3H_4) and their guanidine adducts. The crystal structures and thermal decomposition properties of these organic-molecule-based complex hydrides were carefully investigated. Through metallation, MCN_3H_4 can completely preserve carbon atoms in the system and exhibit a largely improved thermal decomposition compared to CN_3H_5 regarding the extent of C–N bond breaking. By pairing H^+ in CN_3H_5 or MCN_3H_4 with H^- from metal hydrides, the resulting composite can further reduce ammonia libration and promote an endothermic dehydrogenation.

Published by Elsevier Ltd on behalf of Hydrogen Energy Publications LLC.

Introduction

Many hydride systems have been investigated for potential on board vehicular hydrogen storage applications including metal hydrides, complex hydrides, and chemical hydrides. The two main DOE criteria on hydrogen capacities (both gravimetric 5.5 wt.% and volumetric 40 $gH_2\ L^{-1}$) and cycling capabilities (1500 cycles at −40–85 °C and 4 atm) eliminated most of the studied systems [1]. To achieve high storage capacity with minimal weight requires strong chemical bonds between hydrogen and host materials as in metal hydrides (e.g. MgH_2) [2–5], complex hydrides (e.g. $LiBH_4$, $Mg(BH_4)_2$, $LiNH_2$) [6–11], and chemical hydrides (e.g. ammonia borane) [12–14]. To achieve fast cycling at accessible conditions, however, requires weak chemical bonds, fast kinetics, and short diffusion lengths. Thus, the concomitant requirement of

* *Corresponding author.*
E-mail address: huiwu@nist.gov (H. Wu).
http://dx.doi.org/10.1016/j.ijhydene.2016.08.129
0360-3199/Published by Elsevier Ltd on behalf of Hydrogen Energy Publications LLC.

fast recycling is quite challenging for these high-hydrogen-capacity hydride materials.

Small organic hydrogenous molecules or polymers are groups of materials with high hydrogen contents. However thermolysis of these compounds usually results in C–C bond (346 kJ mol^{-1}) instead of C–H bond (411 kJ mol^{-1}) rupture due to the high energy barrier for activating the C–H bond [15–17]. On the other hand, cyclic hydrocarbons and hetero-organic molecules with heteroatoms N, O, S, etc. can be dehydrogenated via the breaking of C–H and/or X–H bonds with the aid of catalysts [18]. A recent study on some primary amines showed promising results on the dehydrogenation properties of these materials at elevated temperatures [19,20]. The composites comprised of primary amines and metal hydrides resemble the extensively studied amide/hydride systems especially with respect to their endothermic dehydrogenation. Therefore, it would be of great interest to study such hybrid systems of inorganic and organic hydrogenous compounds, which show both high hydrogen capacities as well as possible reversibility.

Herein, we report on one of the oldest and the most important small organic molecules, guanidine ($HNC(NH_2)_2$), and its potential application as a hydrogen storage material. Guanidine has played a remarkable role within various chemistry and biochemistry fields. For example, it serves as the central subunit for constructing numerous biomolecules [21]; by coordinating with different organic ligands, the resultant guanidine-based building blocks are essential in supermolecular chemistry [22], etc. Guanidine is a strong base with two amino groups attached to an imine central bond. It contains ~8.5 wt.% hydrogen, which are all protic on amino ($-NH_2$) or imino (–NH) groups. Due to its strongly basic character, the neutral guanidine molecule easily attracts a proton, forming the mesomerism-stabilized guanidinium cation $CN_3H_6^+$. The dehydrogenation of guanidinium borohydride has been studied in both ionic liquid [23] and solid state form [24], displaying an exothermic concomitant H_2 and NH_3 release. In this study, we investigated another ionic form of guanidine, negatively charged guanidinate anion $CN_3H_4^-$. Metalating guanidine by alkali metals leads to the formation of alkali guanidinates [25–27]. The previously reported synthesis of light weight alkali metal guanidinates involved a complicated and expensive reaction of pure alkali metals and guanidine in liquid ammonia in an autoclave under moderate pressure for extended time (e.g. 3–5 days) [25]. Although guanidine was first synthesized more than 150 years ago, its crystal structure was only revealed recently [28,29], and the decomposition properties of guanidine and its related metal guanidinate salts have never been investigated. Furthermore, different from the reported primary amines and metal-hydride composites [19], there is neither C–C bond breaking nor H(C) migration necessary in thermolysis of CN_3H_5. Therefore the thermal decomposition of guanidine and its derivatives would involve a different reaction mechanism. In this paper, we first report on a facile method for synthesizing crystalline lithium and sodium guanidinates and a related guanidine adduct of lithium guanidinate, then discuss their crystal structures, and finally investigate their thermal decomposition properties and mechanism.

Experimental

High-purity guanidine (CN_3H_5) was prepared using a modified method reported in literature [28]. Stoichiometric amount of Na metal and guanidinium carbonate (2:1 M ratio) were separately dissolved in anhydrous ethanol in a nitrogen filled glove box. The two solutions were mixed and filtered to yield a colorless ethanol solution of guanidine. Solid guanidine was obtained by evaporating ethanol under vacuum, and the product was further purified by sublimation on a Schlenk line. The yield for the final purified product was about 60%. The LiH–CN_3H_5 (or $LiNH_2$–CN_3H_5) and NaH–NH_3BH_3 powder mixtures were milled using a Fritsch Pulverisette 7 planetary mill at 200 rpm for 1 h (20 min for the amide mixture) and 200 rpm for 10 min, respectively. After milling, the mixtures were stored in a He-filled glovebox for further structural and property characterizations. All sample handling was performed in the He-filled glovebox due to the air-sensitivity of these complex hydrides.

Phase identification and equilibrium were monitored on samples sealed in 0.7 mm glass capillaries using a Rigaku X-ray diffractometer with a Cu K_α source. Data for structural studies were collected over 24 h at room temperature in the 2θ range of 5–70° with a step size of 0.02°. Rietveld structural refinements were done using the GSAS package [30]. Neutron vibrational spectra (NVS) were measured at 5 K using the BT-4 Filter-Analyzer Neutron Spectrometer (FANS) with the Cu(220) monochromator under conditions that provided energy resolutions of 2–4.5% over the vibrational energy range probed.

Thermogravimetric analysis (TGA) measurements with simultaneous differential scanning calorimetry (DSC) were made with a Netzsch (STA 449 *F1 Jupiter*) TGA-DSC under He flow with Al sample pans and temperature ramp rates of 2 °C/min. Temperature readings were estimated to be accurate to within ±1 °C. Dehydrogenation of CN_3H_5–5LiH was further characterized by temperature-programmed desorption (TPD) performed on a Sieverts-type apparatus described previously [31]. Mass spectrometry (MS) measurements were conducted using a Hiden RGA mass spectrometer. Samples for TPD and MS measurement were heated to 400 °C at 2 °C/min.

The XRD pattern of $LiCN_3H_4 \cdot 2CN_3H_5$ can be indexed using a monoclinic $P2_1$ unit cell with $a = 10.770$ Å, $b = 9.275$ Å, $c = 4.651$ Å, and $\beta = 78.45°$. The crystal structure was then partially solved using direct space methods. Due to the uncertain H positions, First-principles molecular dynamics simulated annealing were performed to confirm the $CN_3H_4^-$ and CN_3H_5 configuration with the lowest energy. Rietveld structural refinement on the optimal structural candidate was done using the GSAS package. The $CN_3H_4^-$ and CN_3H_5 groups were kept as rigid bodies with the C–N and N–H bond lengths and bond angles constrained as the DFT calculated values due to the inadequate number of XRD observations. One $CN_3H_4^-$ and two CN_3H_5 groups together with lattice parameters were refined, yielding the agreement factors of $R_{wp} = 0.0590$, $R_p = 0.0777$, $\chi^2 = 1.712$. The refined XRD pattern is shown in Fig. S2. The crystal structures of $LiCN_3H_4$ and $NaCN_3H_4$ were solved and refined similarly. The Rietveld fit to the XRD pattern of $LiCN_3H_4$ and $NaCN_3H_4$ are shown in Figs. S1 and S3, with $R_{wp} = 0.0284$, $R_p = 0.0364$, $\chi^2 = 1.450$, and $R_{wp} = 0.0940$, $R_p = 0.1253$, $\chi^2 = 1.252$, respectively. More crystallographic

details such as atomic coordinates of these compounds can be found in the corresponding CIFs in ICSD database with number CSD-431825, CSD-431826 and CSD-431827.

First-principles calculations based on density-functional theory (DFT) were performed with the PWSCF package [32]. We used a Vanderbilt-type ultrasoft potential with Perdew-Burke-Ernzerhof exchange correlation. A cutoff energy of 544 eV was found to be enough for the total energy to converge within 0.5 meV/atom. Car-Parrinello molecular dynamics simulations [33] were used to help in searching for the most likely crystal structures. Structure optimizations on the candidate structures were further performed with respect to atomic positions, with the lattice parameters fixed at the experimental values. Lattice dynamics calculations were then performed on the relaxed structures using the supercell method with finite displacements [34].

Results and discussion

Synthesis and crystal structures of guanidinates

Ionization of the neutral molecular guanidine CN_3H_5 can be achieved through reaction between CN_3H_5 and metal hydrides (MH). One protic H^+ from one amino group in CN_3H_5 can be readily attracted by the hydridic H^- from MH, leading to the formation of the $CN_3H_4^-$ anion. The $CN_3H_4^-$ anion can also be obtained by reacting CN_3H_5 with metal amide (MNH_2) with the production of gaseous ammonia.

Crystalline $LiCN_3H_4$ was prepared via ball milling a 1:1 (molar ratio) CN_3H_5–LiH mixture for 1 h as well as a 1:1 CN_3H_5–$LiNH_2$ mixture for 20 min. The X-ray diffraction (XRD) pattern on the final ball milling product can be fitted using a monoclinic structure with $P2_1/c$ symmetry and lattice parameters of $a = 7.2964(8)$ Å, $b = 4.5596(6)$ Å, $c = 9.085(1)$ Å, and $\beta = 103.560(6)^\circ$ (Fig. S1). The crystal structure of $LiCN_3H_4$ (Fig. 1) determined and refined from our room-temperature XRD pattern is consistent with a previous low-temperature single-crystal study [25]. Furthermore, the XRD pattern of CN_3H_4–LiH collected after a shorter time of ball milling (e.g. 30 min) revealed the formation of an intermediate product (Fig. S2), indicating a progressive deprotonating process between CN_3H_5 and LiH. Its XRD pattern could be indexed using a $P2_1$ unit cell with $a = 10.770$ Å, $b = 9.275$ Å, $c = 4.651$ Å, and $\beta = 78.45^\circ$. The volume of the indexed unit cell and the crystal structure solved using combined direct space methods and first-principles molecular dynamics simulated annealing indicated a guanidine adduct of lithium guanidinate with a $Li(CN_3H_4)\cdot 2CN_3H_5$ stoichiometry (Fig. 1). The crystal structure of $Li(CN_3H_4)\cdot 2CN_3H_5$ was then refined based on the XRD pattern, with good agreement (Fig. S2). Likewise, $NaCN_3H_4$ was synthesized via this facile method, i.e., ball milling a 1:1 (molar ratio) CN_3H_5–NaH mixture, but only for 10 min due to a higher reactivity of NaH. $NaCN_3H_5$ adopts a monoclinic structure ($P2_1/c$) with a different cation-anion arrangement compared to $LiCN_3H_5$ (Fig. 1). The refined lattice parameters of $NaCN_3H_5$ at room temperature are $a = 7.9711(8)$ Å, $b = 5.0771(6)$ Å, $c = 9.418(1)$ Å, and $\beta = 110.740(6)^\circ$ and the refined XRD profile is shown in Fig. S3. It should be noted that the refinement based on laboratory X-ray data cannot provide highly accurate atomic coordinates, especially for H. The atomic coordinates of H were obtained from first-principles calculations and the fully relaxed structures are shown in Fig. 1.

In the structure of $LiCN_3H_4$, each Li tetrahedrally coordinates to four $CN_3H_4^-$ anions, with Li–N distances in a range of 2.079–2.113 Å. The two adjacent $Li[CN_3H_4]_4$ tetrahedra coordinating with the same N's form edge-sharing tetrahedra pairs (Fig. 1). Such pairs of Li-tetrahedra were linked through $CN_3H_4^-$ anions and spread over the *bc*-plane, forming infinite layers. The $LiCN_3H_4$ structure is then comprised of these parallel layers running along the *a* axis. $NaCN_3H_4$ possesses a similar monoclinic layered structure with each Na tetrahedrally coordinated to $CN_3H_4^-$ anions (Na–N bond distances ~2.310–2.443 Å). Whereas, within each layer, the neighboring $Na[CN_3H_4]_4$ tetrahedra were corner-sharing at the same N moieties (Fig. 1). Different from $LiCN_3H_4$ and $NaCN_3H_4$, in the $LiCN_3H_4\cdot 2CN_3H_5$ structure, each Li tetrahedrally coordinates to two $CN_3H_4^-$ anions and two CN_3H_5 molecules. The $CN_3H_4^-$ anions serve as the bridging ligands, connecting all these Li-tetrahedra to a chain-like cluster along the *c* direction. The whole structure is then built up from these isolated $LiCN_3H_4\cdot 2CN_3H_5$ chain clusters (Fig. 1).

The charge distribution among all atoms is also changed upon deprotonating CN_3H_5 to $CN_3H_4^-$. From the Mulliken population analysis based on first-principles calculations (Table S1), the H's in CN_3H_5 are much more positively charged before ionization, indicating their proclivity to react with the H^- from MH. After forming $CN_3H_4^-$, both C and H become less positively charged with almost no electron density change in N, which results in less polarized C–N bonds and N–H bonds in the imino group but more polarized N–H bonds in the amino group in MCN_3H_4. The structure and bonding environment of MCN_3H_4 are further investigated by neutron vibrational spectroscopy (Fig. 2 and Fig. S4). The first-principles calculated NVS are also shown in Fig. 2 and Fig. S4. For MCN_3H_4, the observed phonon bands can be assigned to the rocking and librational modes of C–N (~70 meV) and scissoring modes of C–NH bonds (~76 meV); librational modes of N–H (~80–87 meV); bending modes of C–N bonds (~90–92 meV); bending modes of N–H (~99–109 meV); stretching mode of C–NH_2 bonds (111–112 meV); bending modes of N–H in NH_2 (120–124 meV); stretching mode of C–NH bonds (144–145 meV); rocking modes of N–H (149–152 meV); stretching and deformation modes of C–N (175–180 meV) and NH_2 scissoring modes (199 meV). In general, the calculated spectra agree reasonably well with the observed NV spectra for both compounds, and thus further support the validity of our determined structures. Of the two calculated asymmetric N–H stretching modes from the $-NH_2$ amino groups (380 meV and 410 meV), the lower energy is for the H showing the nearest distance with N in the neighboring $CN_3H_4^-$ and the higher energy is for the other H in the same amino group, which does not have such a close H-bond interaction. The calculated stretching modes in the –NH imino group where N is jointly shared by two cations (417 meV), and in the –NH where NH is coordinated by only one cation (420 meV) seem to be in similar energy ranges as those reported for CN_3H_5 [28] and primary amine/hydride composites [19], suggesting a similar N–H bonding strength in these compounds. However the lower energy (380 meV) of the

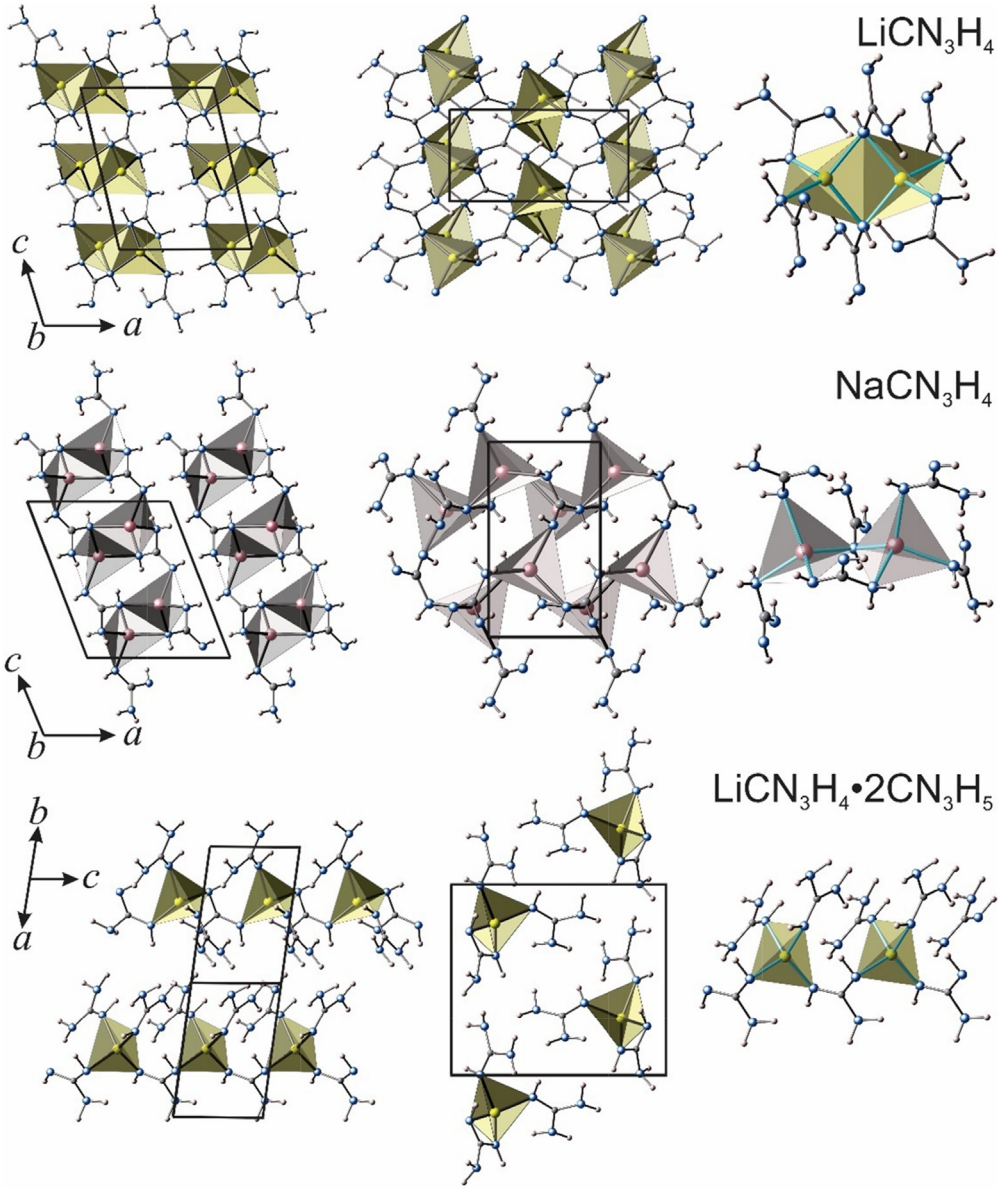

Fig. 1 – Crystal structures of $LiCN_3H_4$, $NaCN_3H_4$, and $LiCN_3H_4{\cdot}2CN_3H_5$. (Left column) MCN_3H_4 layers or chains along the *a* or *c* axis; (middle column) views along a or *c* axis, showing the in-layer tetrahedra connections for MCN_3H_4 and the isolated chain clusters for $LiCN_3H_4{\cdot}2CN_3H_5$; and (right column) different local cation coordination environments and M-tetrahedra arrangements. Li, Na, C, N and H are represented by yellow, pink, grey, blue and white spheres, respectively. (For interpretation of the references to color in this figure legend, the reader is referred to the web version of this article.)

asymmetric N–H stretching from the amino group in $CN_3H_4^-$ is much less than those in metal amides (MNH_2) (characteristic lower end of N–H asymmetric stretching mode energies in MNH_2 are ~404 meV), indicating a weaker N–H bonding of the $-NH_2$ group in MCN_3H_4.

Thermal decomposition of guanidinates

Thermal decomposition of guanidine and these guanidinates were investigated using thermogravimetry analysis (Fig. 3 and Fig. S5) and the qualitative gas desorption from these compounds were characterized using a mass spectrometer. Guanidine (CN_3H_5) completely decomposes (>95 wt.% loss) in the temperature range of 170–350 °C, releasing a mixture of NH_3, CH_4, H_2 (trace) and N_2 (trace) gases (Fig. 4). No hydrogen cyanide (CNH) or hydrazine (N_2H_4) gases were observed in the measured temperature range. These observations indicate a majority of bond-breaking of C–N bonds rather than of N–H bonds during thermolysis of CN_3H_5 due to the weaker C–N bonds (305 kJ mol^{-1}) than N–H bonds (386 kJ mol^{-1}).

$LiCN_3H_4$ shows much less weight loss than that of CN_3H_4, albeit still significant at elevated temperatures (~30 wt.%) from ~220 to 270 °C (Fig. 3). Mass spectra indicate the weight loss is mostly due to ammonia release. There is also a small amount of H_2 observed during decomposition of $LiCN_3H_4$ (Fig. 4). In contrast to CN_3H_5, little CH_4 was observed in the MS spectra,

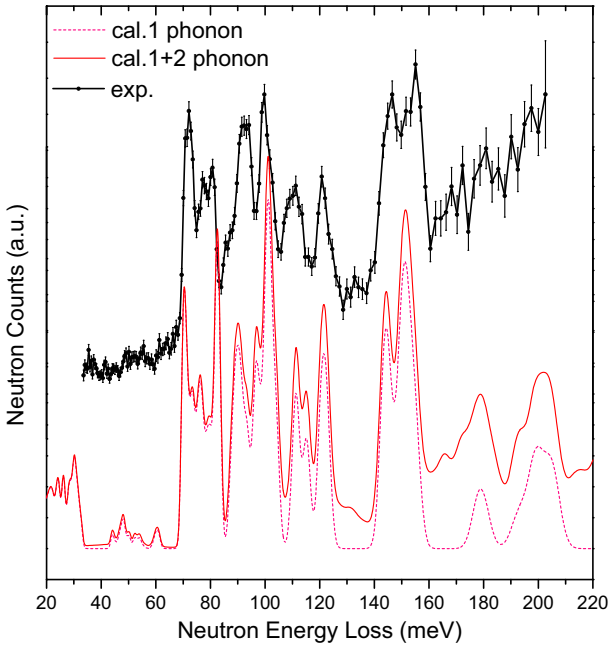

Fig. 2 – Neutron vibrational spectra and the calculated phonon modes of $LiCN_3H_4$.

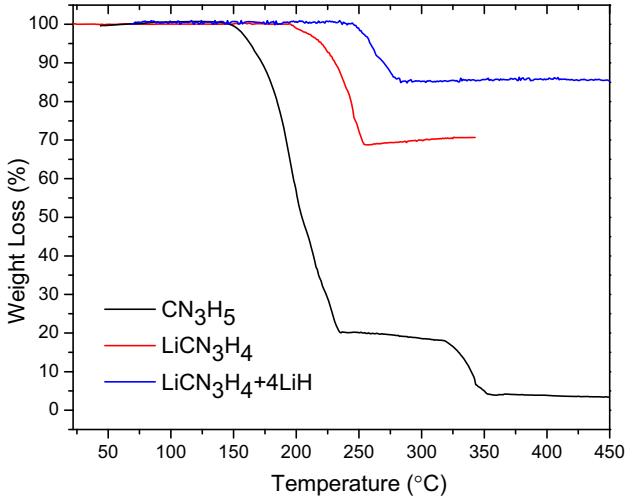

Fig. 3 – TGA weight loss of CN_3H_5, $LiCN_3H_4$ and $LiCN_3H_4$–4LiH with 2 °C/min heating rate to 450 °C.

suggesting metalation stabilizes the CN_3H_5 molecule (as also reflected in the less polarized C–N bonds from the charge population analysis) and mitigates the extent of C–N bond dissociation. The XRD pattern collected on the decomposition residue of $LICN_3H_4$ shows the formation of lithium cyanamide (Li_2CN_2, Fig. S6), which was further confirms the preservation of C/N species by the formation of more stable decomposition products. Li_2CN_2 was also observed in the decomposition product of $LiBH_4$–CN_3H_5 system in our recent study [35].

Since $LiCN_3H_4$ by itself could not dehydrogenate and liberate H_2, a $LiCN_3H_4$–4LiH composite was then prepared, which contains equal amounts of the oppositely charged H, aiming to suppress ammonia and ameliorate H_2 release. TGA results indeed show a significantly reduced weight loss from

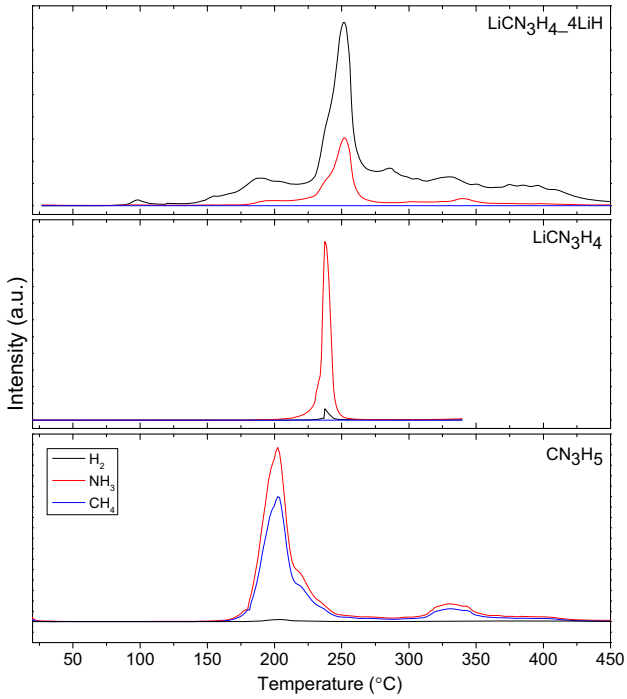

Fig. 4 – MS results from decomposition of CN_3H_5, $LiCN_3H_4$, and $LiCN_3H_4$–4LiH with 2 °C/min heating rate to 400 °C.

the $LiCN_3H_4$–4LiH mixture consistent with the mass spectra result where H_2 is the major component among the released gases (Figs. 3 and 4). Note: pure LiH decomposes and releases H_2 only at >600 °C.

The $LiCN_3H_4$–4LiH composite was further studied in detail to understand the mechanism of its dehydrogenation. Since $LiCN_3H_4$ is made from a 1:1 ratio of CN_3H_5/LiH, the dehydrogenation from the composite of CN_3H_5/5LiH was then directly measured. During volumetric temperature-programmed desorption (TPD), CN_3H_5/5LiH composite decomposes initially at 90 °C and releases ~1 H_2 equiv. per mol CN_3H_5 (Fig. 5). The MS indicates an exothermic pure H_2 release in this temperature range (Fig. 5 and Fig. S7), which is consistent with the formation of $LiCN_3H_4$ according to Eq. (1).

$$CN_3H_5 + LiH \rightarrow LiCN_3H_4 + H_2 \quad (1)$$

The production of $LiCN_3H_4$ from CN_3H_4 and LiH is irreversible, somewhat revealing its stability. With increasing temperature, both TPD and MS show irregular desorption profiles, starting from ~150 °C with a subsequent sharp gas release peaked at ~260 °C. In this later desorption event, H_2 is still the major component but accompanied by a noticeable amount of NH_3. Such desorption behavior is nearly the same as that of the $LiCN_3H_4$/4LiH composite (Fig. 4) and further confirms that $LiCN_3H_4$ is produced during the first H_2 gas release event. Furthermore, from DCS measurement, different from the 1st H_2 release event, the desorption in the higher-temperature range is mildly endothermic (Fig. S7).

Since the second H_2 release event of the composite starts at much lower temperature (150 °C) than that of the pristine

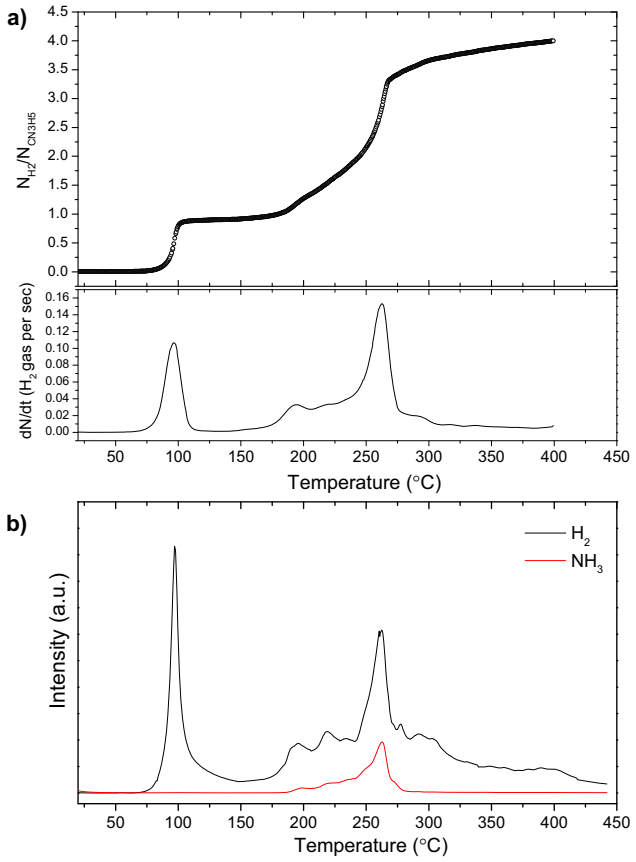

Fig. 5 – a) TPD results of the CN_3H_5–5LiH composite with 2 °C/min heating rate to 400 °C. The amount of H_2 gas released (top panel) has been normalized as n (H_2 gas)/mol CN_3H_5; b) MS results of CN_3H_5–5LiH composite with 2 °C/min heating rate to 400 °C.

$LiCN_3H_4$, $LiCN_3H_4$ formed *in-situ* should first directly react with LiH and emit one H_2 through an H^+ and H^- combination process [36,37].

$$LiCN_3H_4 + LiH \rightarrow Li_2CN_3H_3 + H_2 \quad (2)$$

This echoes the fact of the more polarized N–H bond in $-NH_2$ calculated from the Mulliken charge distribution and the weaker N–H bond in the amino group of $LiCN_3H_4$ observed in NVS compared to MNH_2, suggesting H in the amino group should dehydrogenate first. With increasing temperature and the observed concurrence of H_2 and NH_3, the intermediate $Li_2CN_3H_3$ should either react with the remaining LiH to liberate H_2 (Eq. (3)), or decompose to Li_2CN_2 and NH_3 (Eq. (4)). Such dehydrogenation and deammoniation processes compete in this temperature range.

$$\text{Dehydrogenation: } Li_2CN_3H_3 + LiH \rightarrow Li_3CN_3H_2 + H_2 \quad (3)$$

$$Li_3CN_3H_2 + LiH \rightarrow Li_4CN_3H + H_2$$

$$Li_4CN_3H + LiH \rightarrow Li_5CN_3 + H_2$$

$$\text{Deammoniation: } Li_2CN_3H_3 \rightarrow Li_2CN_2 + NH_3 \quad (4)$$

If these two reactions occur, we should observe the formation of Li_4CN_3H/Li_5CN_3 and Li_2CN_2 after decomposition completes. However, the XRD pattern collected on the decomposition residue of CN_3H_5/5LiH clearly shows a mixture of Li_2CN_2, Li_2NH and LiH (Fig. S8), which implies that more complicated reactions emerge in this temperature range.

As evidenced by the presence of NH_3 in the mass spectra and Li_2NH/LiH residues in the decomposition products, an ammonia-mediated mechanism may also play a role in the current system, as proposed in the amide/hydride systems [38,39], e.g. $LiNH_2$/LiH. The ammonia generated from Eq. (4) can react with the excess LiH present in the system following the chain reactions reported in the literature [38], and can be simplified as:

$$NH_3 + LiH \rightarrow LiNH_2 + H_2 \quad (5)$$

$$LiNH_2 + LiH \rightarrow LiH + \tfrac{1}{2}NH_3 + \tfrac{1}{2}Li_2NH \rightarrow \ldots. \rightarrow Li_2NH + H_2 \quad (6)$$

The temperature range for the second gas desorption event in the current system (~200–400 °C) is consistent with the dehydrogenation temperature of the $LiNH_2$/LiH composite. Therefore, after the initial direct combination of $LiCN_3H_4$ and LiH at 150 °C, a subsequent ammonia-mediated mechanism is highly likely in the CN_3H_5/5LiH composite. The concurrence of Eqs. (4)–(6) also explains the upper shift of the desorption peak (i.e. 260 °C) of CN_3H_5/5LiH compared to that of $LiCN_3H_4$.

In Fig. 5, after the concomitant peak of NH_3 and H_2, it is interesting that only H_2 liberates from the system at higher temperatures (>270 °C). This resembles the MS signal of $LiCN_3H_4$, where no more NH_3 releases after the sharp NH_3 peak at ~238 °C. Therefore, in CN_3H_5/5LiH after the complete deammoniation from $LiCN_3H_4$ formed *in-situ* (Eq. (4)), the remaining dehydrogenation should follow Eq. (6) between the remaining LiH and the $LiNH_2$ produced in Eq. (5). For the complete decomposition process of CN_3H_5/5LiH up to 450 °C, a final reaction equation can be obtained by summing Eqs. (1), (2), (4)–(6):

$$CN_3H_5 + 5LiH \rightarrow Li_2CN_2 + Li_2NH + LiH + 4H_2 \quad (7)$$

The total amount of H_2 release agrees well with the TPD measurement (Fig. 5). From Eqs. (1), (2), and (5), only three equiv. LiH were used, the remaining LiH should be in large excess to react with $LiNH_2$ in Eq. (6), which may explain why little ammonia was observed after 270 °C. Finally, although later desorption from the $LiCN_3H_4$/4LiH mixture is endothermic, the loss of NH_3 prevents a complete H_2 restoration.

Previous studies have shown that increasing Li^+ ion mobility would help reduce the dehydrogenation temperature and NH_3 liberation [40–42], which will promote a direct amide/hydride reaction rather than the ammonia-mediated process. In the $LiCN_3H_4$ structure, Li is tightly linked by N from four surrounding $CN_3H_4^-$ anions, and there are no structural channels or cation vacancies for Li^+ ions

to migrate. Therefore, the CN_3H_5/5LiH composite shows noticeable NH_3 emission and an ammonia-mediated dehydrogenation mechanism at high temperatures. Different approaches have been used to facilitate dehydrogenation (e.g. Eq. (3)) and suppress NH_3 generation: i) weakening the N–H bonds by introducing cations with higher electronegativity [43] such as Mg^{2+} so as to promote the H^+ and H^- combination, e.g. Eq. (3); ii) introducing more reactive H^--containing hydrides such as borohydrides. The results of these related projects will be reported in subsequent papers.

Through ionization we have successfully demonstrated the modification on the thermal decomposition behavior of guanidine. Due to the endothermic nature of N–H bond-breaking or even C–H bond-breaking in organic molecules during dehydrogenation, organic-molecule-based complex hydrides would open up a new direction for developing reversible hydrogen storage systems with high-H capacities.

Conclusions

We successfully prepared the anion form of guanidine, $CN_3H_4^-$, through a facile reaction of guanidine with alkali-metal hydrides (LiH, NaH) or amide ($LiNH_2$). The crystal structures of the resulting alkali-metal guanidinates, i.e. $LiCN_3H_4$ and $NaCN_3H_4$, and their guanidine adducts, i.e. $LiCN_3H_4{\cdot}2CN_3H_5$ were investigated using combined XRD and molecular dynamics simulated-annealing methods. Metal guanidinates MCN_3H_4 exhibit largely improved thermal decomposition properties compared to CN_3H_5 in terms of the alleviated extent of C–N bond-breaking. By further pairing the H^+ from CN_3H_5 or $LiCN_3H_4$ with the H^- from metal hydrides, i.e. LiH, the resulting composite system is able to convert the dominant deammoniation of MCN_3H_4 during thermolysis to major endothermic dehydrogenation. Detailed investigation into the dehydrogenation mechanism suggests that both CN_3H_5/5LiH and $LiCN_3H_4$/4LiH composites dehydrogenate initially via the direct combination reaction of H^+ and H^- at low temperature and then through an ammonia-mediated pathway at high temperatures. To enhance the potential of these materials for hydrogen storage, future studies need to focus on more effectively promoting hydrogenation by the further activation of H^+, the weakening of the N–H bond in MCN_3H_4, and/or the introduction of more reactive H^- into the system.

Funding sources

This work was partially supported by the DOE-EERE Grant No. DE-EE0002978 (T.J.U.).

Notes

Certain commercial suppliers are identified in this paper to foster understanding. Such identification does not imply recommendation or endorsement by the NIST.

Acknowledgments

We would like to thank Dr. Qiang Ye (NCNR, NIST) for his assistance with the mass spectrometer setup.

Appendix A. Supplementary data

Supplementary data related to this article can be found at http://dx.doi.org/10.1016/j.ijhydene.2016.08.129.

REFERENCES

[1] Targets for onboard hydrogen storage systems for light-duty vehicles. US Department of Energy, Office of Energy Efficiency and Renewable Energy and The FreedomCAR and Fuel Partnership; September 2009. http://www1.eere.energy.gov/hydrogenandfuelcells/storage/pdfs/targets_onboard_hydro_storage.pdf.

[2] Vajo JJ, Mertens F, Ahn CC, Bowman Jr RC, Fultz B. Altering hydrogen storage properties by hydride destabilization through alloy formation: LiH and MgH_2 destabilized with Si. J Phys Chem B 2004;108:13977–83.

[3] Wu H, Zhou W, Udovic TJ, Rush JJ, Yildirim T. Structure and vibrational spectra of calcium hydride and deuteride. J Alloys Compd 2007;436:51–5.

[4] Wu H, Zhou W, Udovic TJ, Rush JJ. Hydrogen storage in a novel destabilized hydride system, Ca_2SiH_x: effect of amorphilization. Chem Mater 2007;19:329–34.

[5] Wu H, Zhou W, Udovic TJ, Rush JJ, Yildirim T. Crystal chemistry of perovskite-type hydride $NaMgH_3$: implications for hydrogen storage. Chem Mater 2008;20:2335–42.

[6] Vajo JJ, Skeith S, Mertens F. Reversible storage of hydrogen in destabilized $LiBH_4$. J Phys Chem B 2005;109:3719–22.

[7] Chong M, Mastuo M, Orimo S, Autrey T, Jensen C. Selective reversible hydrogenation of $Mg(B_3H_8)_2/MgH_2$ to $Mg(BH_4)_2$: pathway to reversible borane-based hydrogen storage? Inorg Chem 2015;54:4120–5.

[8] Chen P, Xiong Z, Luo J, Lin J, Tan K. Interaction of hydrogen with metal nitrides and imides. Nature 2002;420:302–4.

[9] Wu H, Zhou W, Udovic TJ, Rush JJ, Yildirim T. Structures and crystal chemistry of Li_2BNH_6 and $Li_4BN_3H_{10}$. Chem Mater 2008;20:1245–7.

[10] Huang Z, Chen X, Yisgedu T, Zhao JC, Shore SG. High-capacity hydrogen release through hydrolysis of NaB_3H_8. Int J Hydrogen Energy 2011;36:7038–42.

[11] Huang Z, King G, Chen X, Hoy J, Yisgedu T, Lingam HK, et al. A simple and efficient way to synthesize unsolvated sodium octahydrotriborate. Inorg Chem 2010;49:8185–7.

[12] Huang Z, Autrey T. Boron-nitrogen-hydrogen (BNH) compounds: recent developments in hydrogen storage, applications in hydrogenation and catalysis and new syntheses. Energy Environ Sci 2012;5:9257–68.

[13] Chen X, Gallucci J, Campana C, Huang Z, Lingam HK, Shore SG, et al. Anti and gauche conformers of an inorganic butane analogue, $NH_3BH_2NH_2BH_3$. Chem Comm 2012;48:7943–5.

[14] Huang Z, Lingam HK, Chen X, Porter SH, Duo A, Woodard PM, et al. Synthesis, structural analysis, and thermal decomposition studies of $[(NH_3)_2BH_2]B_3H_8$. RSC Adv 2013;3:7460–5.

[15] Cottrell TL. The strengths of chemical bonds. 2nd ed. London: Butterworths; 1958.

[16] Darwent B deB. National standard reference data series. Washington DC: National Bureau of Standards, No. 31; 1970.
[17] Benson SW. III- bond energies. J Chem Educ 1965;42:502.
[18] Shilov AE, Shulpin GB. Activation of C-H bonds by metal complexes. Chem Rev 1997;97:2879–932.
[19] Chen J, Wu H, Wu G, Xiong Z, Wang R, Fan J, et al. Lithiated primary amine-a new material for hydrogen storage. Chem Eur J 2014;20:6632–5.
[20] Chen J, Wu G, Xiong Z, Wu H, Chua YS, Zhou W, et al. Synthesis, thermal behaviour, and dehydrogenation kinetics study of lithiated ethylenediamine. Chem Eur J 2014;42:13636–43.
[21] Beyer H, Walter W. Lehrbuch der Organischen Chemie. 24th ed. Stuttgart: Hirzel Verlag; 2004.
[22] Müller IM, Möller D. A new ligand for the formation of triangular building blocks in supramolecular chemistry. Eur J Inorg Chem 2005;2005:257–63.
[23] Doroodian A, Dengler JE, Genest A, Rosch N, Rieger B. Methylguanidinium borohydride: an ionic-liquid-based hydrogen-storage material. Angew Chem Int Ed 2010;49:1871–3.
[24] Groshens TJ, Hollins RA. New chemical hydrogen storage materials exploiting the self-sustaining thermal decomposition of guanidinium borohydride. Chem Commun 2009:3089–91.
[25] Hoepfner V, Dronskowski R. $RbCN_3H_4$: the first structurally characterized salt of a new class of guanidinate compounds. Inorg Chem 2011;50:3799–803.
[26] Sawinski PK, Dronskowski R. Solvothermal synthesis, crystal growth, and structure determination of sodium and potassium guanidinate. Inorg Chem 2012;51:7425–30.
[27] Sawinski PK, Deringer V, Dronskowski R. Completing a family: $LiCN_3H_4$, the lightest alkali metal guanidinate. Dalton Trans 2013;42:15080–7.
[28] Gobel M, Klapotke TM. First structural characterization of guanidine, $HN{=}C(NH_2)_2$. Chem Comm 2007:3180–2.
[29] Yamada T, Liu X, Englert U, Yamane H, Dronskowski R. Solid state structure of free base guanidine achieved at last. Chem Eur J 2009;15:5651–5.
[30] Larson AC, Von Dreele RB. General structure analysis system. Report LAUR 86-748. NM: Los Alamos National Laboratory; 1994.
[31] Zhou W, Wu H, Hartman MR, Yildirim T. Hydrogen and methane adsorption in metal-organic frameworks: a high-pressure volumetric study. J Phys Chem C 2007;111:16131–7.
[32] Giannozzi P, Baroni S, Bonini N, Calandra M, Car R, Cavazzoni C, et al. Quantum ESPRESSO: a modular and open-source software project for quantum simulations of materials. J Phys Condens Matter 2009;21:395502.
[33] Car R, Parrinello M. Unified approach for molecular dynamics and density-functional theory. Phys Rev Lett 1985;55:2471–4.
[34] Kresse G, Furthmuller J, Hafner J. Ab initio force constant approach to phonon dispersion relations of diamond and graphite. Europhys Lett 1995;32:729.
[35] Wu H, Zhou X, Rodriguez EE, Zhou W, Udovic TJ, Yildirim T, et al. A new family of metal borohydride guanidinate complexes: synthesis, structures and hydrogen-storage properties. J Solid State Chem 2016;242:186–92.
[36] Chen P, Xiong Z, Luo J. Interaction between lithium amide and lithium hydride. J Phys Chem B 2003;107:10967–70.
[37] Chen P, Xiong Z, Yang L, Wu G, Luo W. Mechanistic investigations on the heterogeneous solid-state reaction of magnesium amides and lithium hydrides. J Phys Chem B 2006;110:14221–5.
[38] Ichikawa T, Hanada N, Isobe S. Mechanism of novel reaction from $LiNH_2$ and LiH to Li_2NH and H_2 as a promising hydrogen storage system. J Phys Chem B 2004;108:7887–92.
[39] Hu YH, Ruckenstein E. Ultrafast reaction between LiH and NH_3 during H_2 storage in Li_3N. J Phys Chem A 2003;107:9737–9.
[40] Wu H. Structure of ternary imide $Li_2Ca(NH)_2$ and hydrogen storage mechanisms in amide-hydride systems. J Am Chem Soc 2008;130:6515–22.
[41] Wu H. Strategies for the improvement of hydrogen storage properties of metal hydride materials. ChemPhysChem 2008;9:2157–62.
[42] Cao H, Wang J, Chua Y, Wang H, Wu G, Xiong Z, et al. NH_3 mediated or ion migration reaction: the case study on halide-amide system. J Phys Chem C 2014;118:2344–9.
[43] Orimo S, Nakamori Y, Kitahara G. Destabilization and enhanced dehydriding reaction of $LiNH_2$: an electronic structure viewpoint. Appl Phys A 2004;79:1765–7.

Supporting Information

Development of potential organic-molecule-based hydrogen storage materials: Converting the C-N bond-breaking thermolysis of guanidine to N-H bond-breaking dehydrogenation

Xiuquan Zhou,[a] Wei Zhou,[b] Terrence J. Udovic,[b] Taner Yildirim,[b] John J. Rush,[bc] Efrain E. Rodriguez,[a] and Hui Wu[b]*

[a]*Department of Chemistry & Biochemistry, University of Maryland, College Park, Maryland, 20742-4454, USA.*

[b]*NIST Center for Neutron Research, National Institute of Standards and Technology, Gaithersburg, Maryland 20899-6102, USA.*

[c] *Department of Materials Science and Engineering, University of Maryland, College Park, Maryland, 20742-2115, USA.*

Email: huiwu@nist.gov

Table S1. Mulliken Population Analysis of Charge Densities

	CN_3H_5	$LiCN_3H_4$	$NaCN_3H_4$
	crystal	crystal	crystal
C	+0.44, +0.45	+0.32	+0.31
N1 (amino)	-0.84, -0.82, -0.83, -0.81	-0.80	-0.79
H1 (amino)	+0.41, +0.43, +0.40, +0.41	+0.28	+0.29
H2 (amino)	+0.39, +0.40, +0.42, +0.40	+0.30	+0.31
N2 (imino)	-0.81, -0.81	-0.80	-0.80
H3(imino)	+0.39, +0.38	+0.26	+0.25
N3 (imino shared by two M's)	-	-0.80	-0.81
H4 (imino)	-	+0.24	+0.24
Li or Na		+1.00	+1.00

Figure S1. Experimental (circles), calculated (line), and difference (line below observed and calculated patterns) XRD profiles for $LiCN_3H_4$ at room temperature (CuKa radiation). Vertical bars indicate the calculated positions of Bragg peaks. R_{wp}=0.0284, R_p=0.0364, χ^2=1.450.

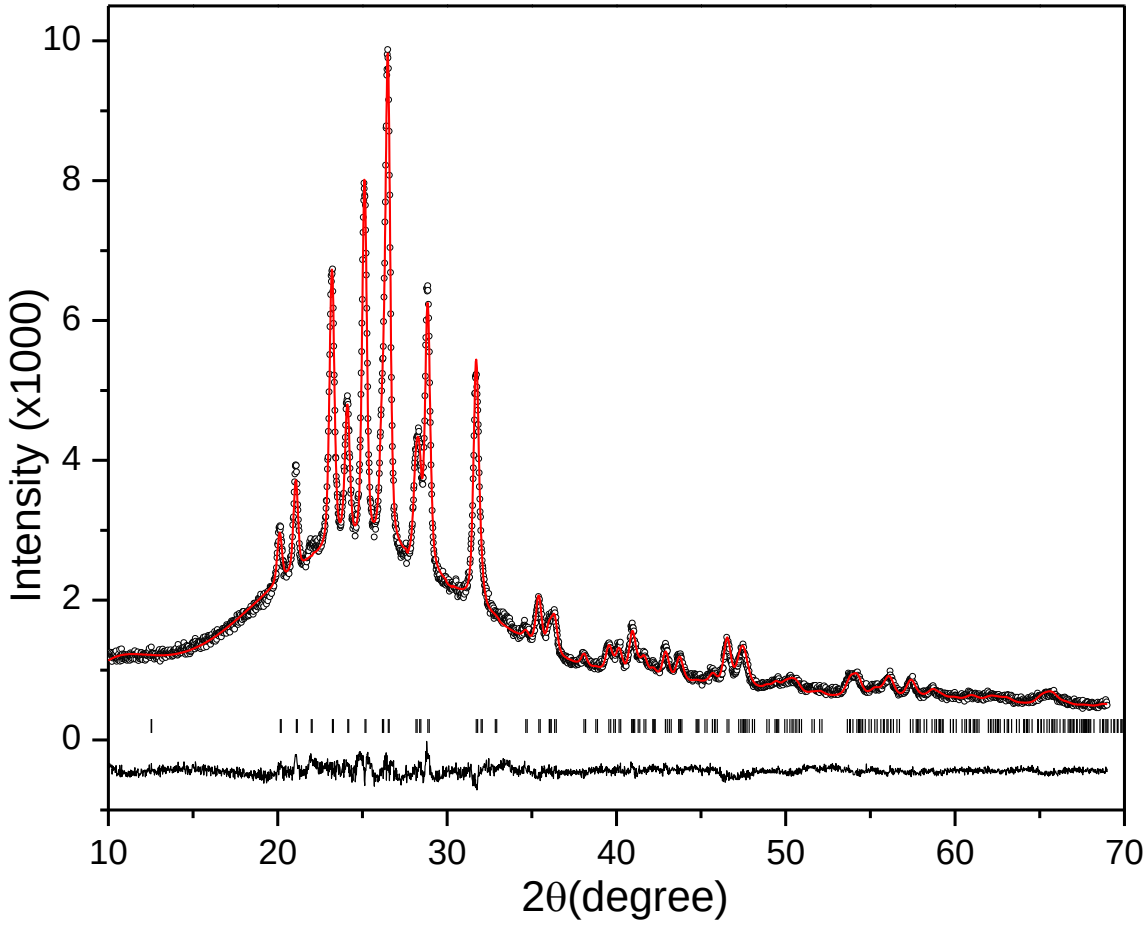

Figure S2. Experimental (circles), calculated (line), and difference (line below observed and calculated patterns) XRD profiles for $LiCN_3H_4 \cdot 2CN_3H_5$ at room temperature. Vertical bars indicate the calculated positions of Bragg peaks from $LiCN_3H_4 \cdot 2CN_3H_5$ (72.60(9) wt. %), unreacted precursors CN_3H_5 (12.0(2) wt. %) and LiH (5.6(3) wt. %), and already formed $LiCN_3H_4$ (9.8(2) wt. %) (from the top). R_{wp}=0.0590, R_p=0.0777, χ^2=1.712.

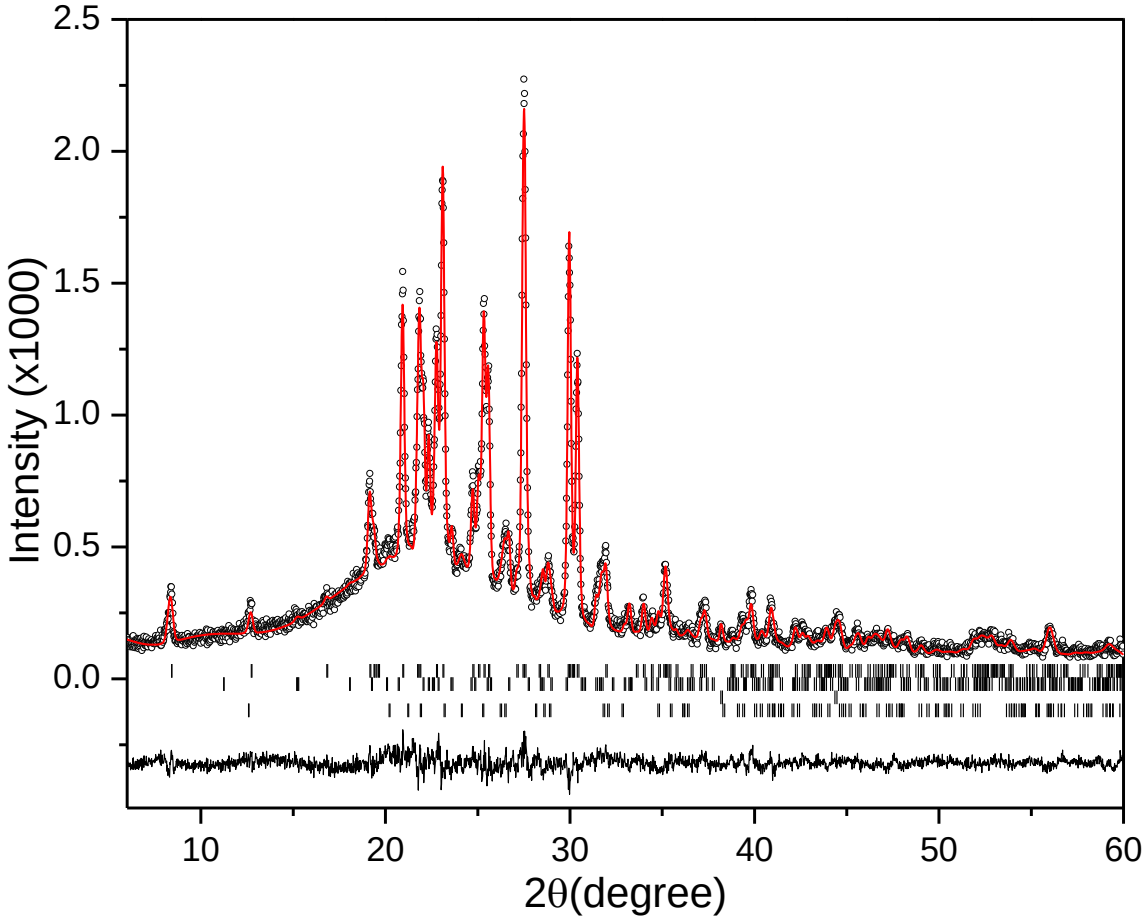

Figure S3. Experimental (circles), calculated (line), and difference (line below observed and calculated patterns) XRD profiles for $NaCN_3H_4$ at room temperature. Vertical bars indicate the calculated positions of Bragg peaks. R_{wp}=0.0940, R_p=0.1253, χ^2=1.252.

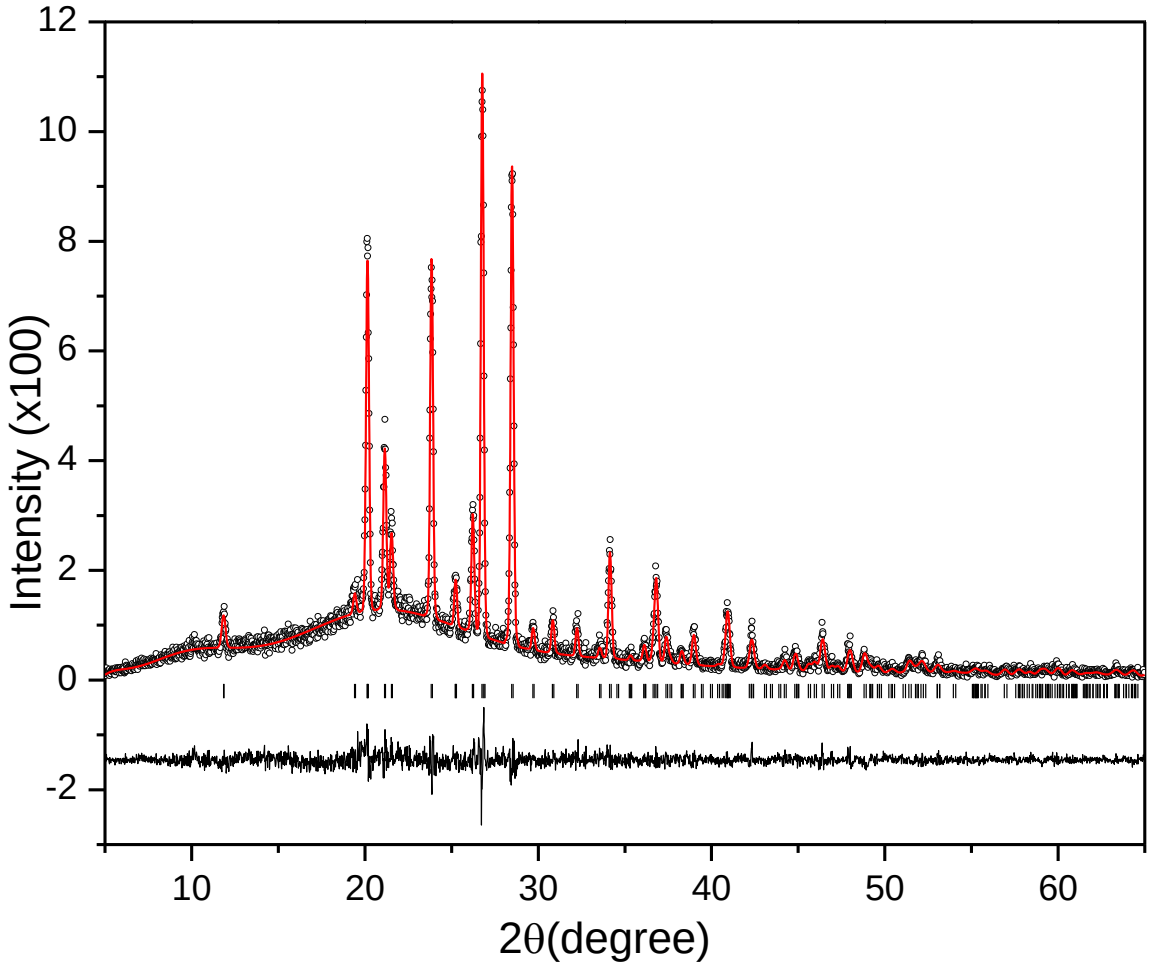

Figure.S4 Neutron vibrational spectra and the calculated phonon modes of $NaCN_3H_4$.

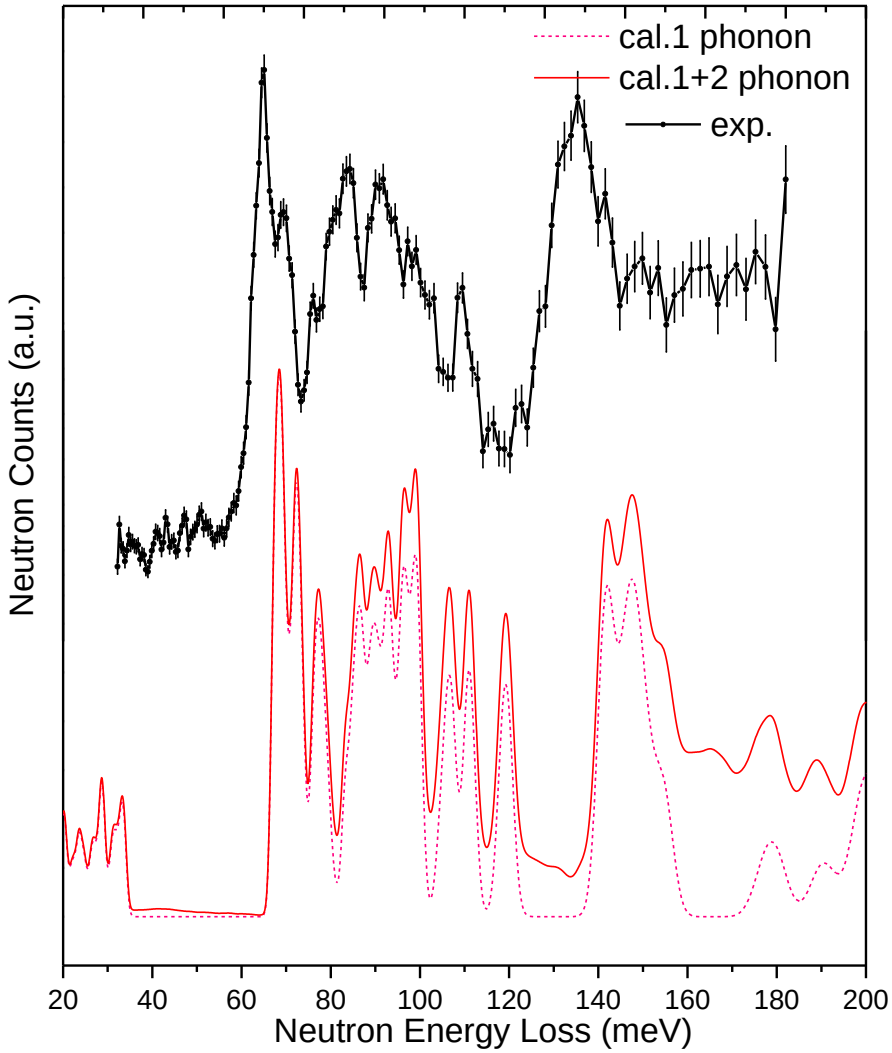

Figure S5. TGA and MS weight loss of $NaCN_3H_4$ with 2 °C/min heating rate to 400 °C.

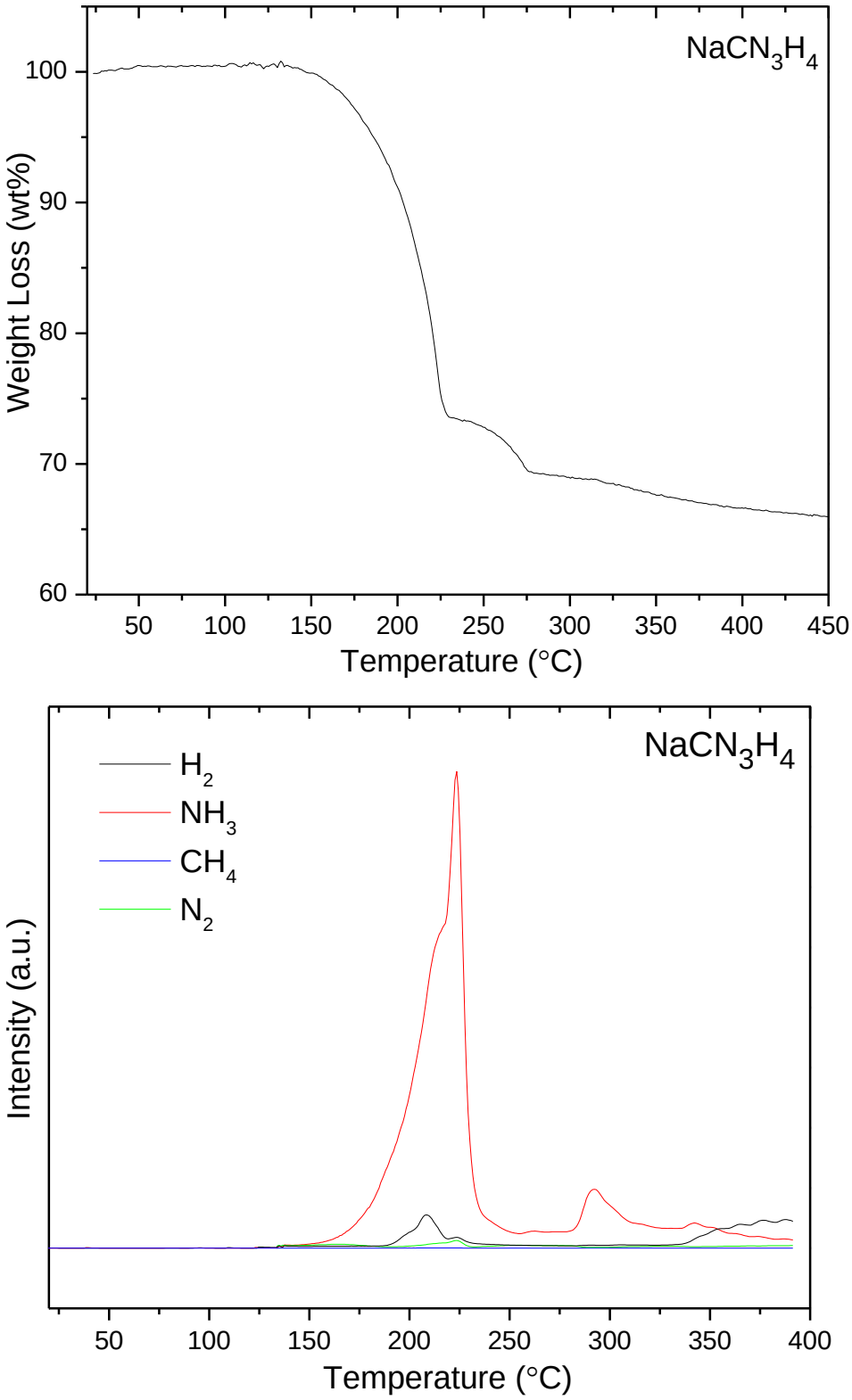

Figure S6. XRD pattern of the residue of $LiCN_3H_4$ after thermal decomposition up to 400°C. Besides Li_2CN_2 there are peaks that cannot match any known phase in the Li-C-N-H quaternary phase diagram or be indexed using a single phase.

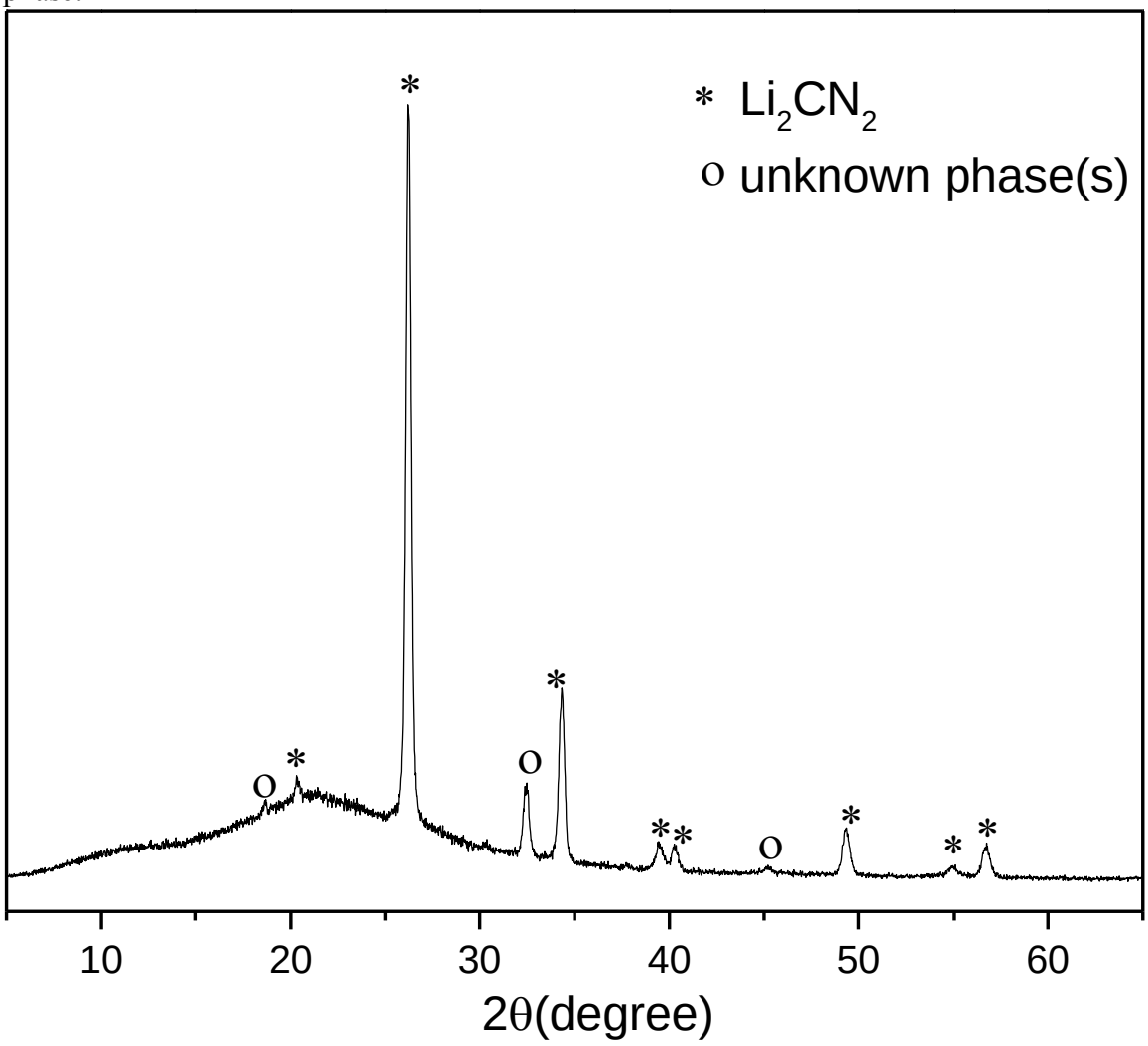

Figure S7. DSC result of thermal decomposition of $LiCN_3H_4$ and CN_3H_5-5LiH with 2 °C/min heating rate to 450 °C.

.

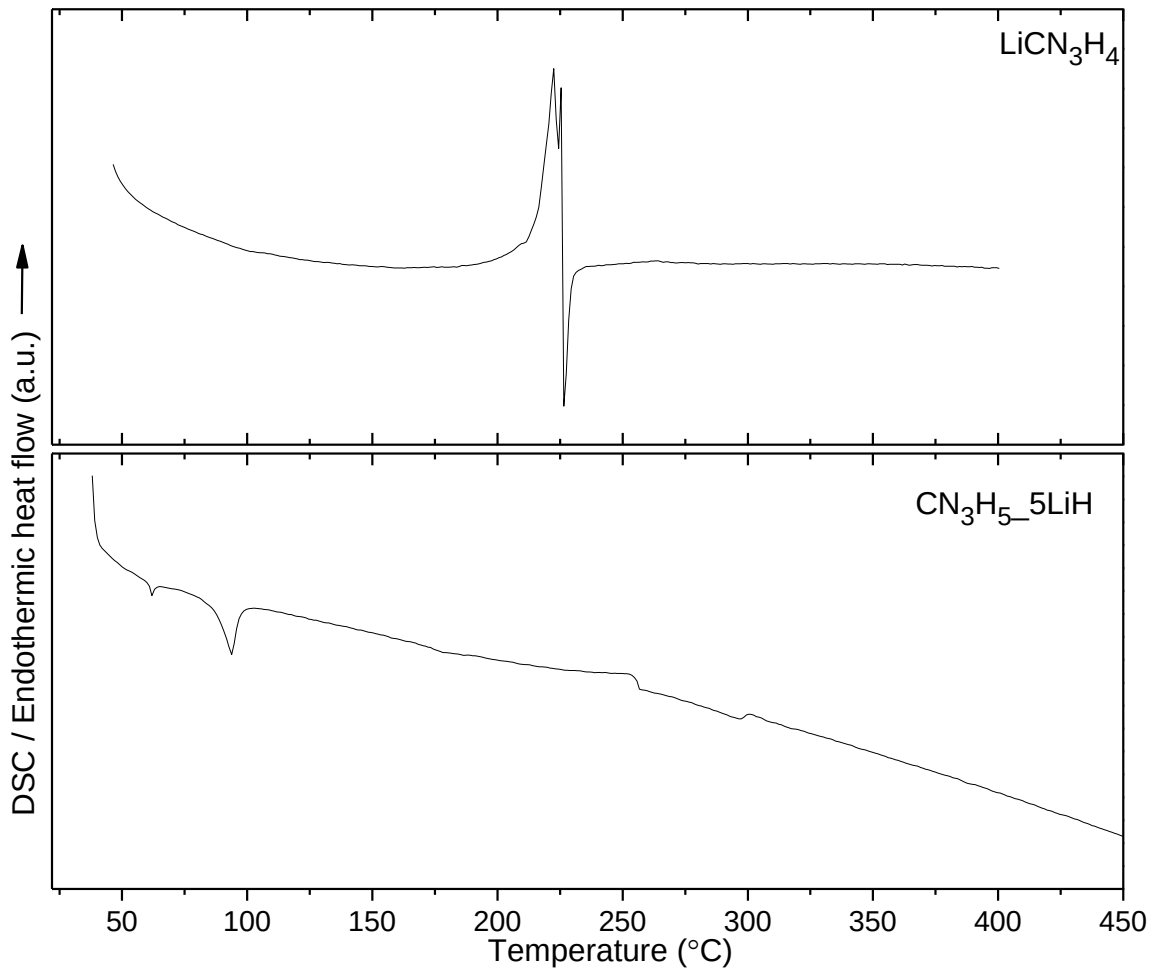

Figure S8. XRD pattern on the residue of CN_3H_5-5LiH after thermal decomposition up to 400 °C.